RSC Advances

PAPER

View Article Online
View Journal | View Issue

Cite this: *RSC Adv.*, 2019, **9**, 2011

A solid-state chemical method for synthesizing MgO nanoparticles with superior adsorption properties†

Hongyu Zhang, Jindou Hu, Jing Xie, Shiqiang Wang and Yali Cao *

As a traditional and effective adsorbent, MgO is a low-cost, eco-friendly, nontoxic, and economical material for wastewater treatment. However, multistep processing and the use of organic agents result in high costs and lead to environmental pollution, strongly inhibiting the practical application of MgO. Herein, a simple solid-state chemical route has been used to prepare small-sized MgO nanoparticles with a large specific surface area of 213 $m^2\ g^{-1}$ without using liquid solvents, template agents, or surfactants. This facile method is a green strategy that is suitable for large-scale production, avoiding complex preparation processes and serious environmental pollution. The obtained small-sized MgO nanoparticles showed a superior adsorption capacity of 2375 mg g^{-1} towards Congo red, originating from the large specific surface area and surface features (hydrogen bonds and electrostatic interactions). The adsorption behavior obeyed a pseudo-second-order rate equation and the Langmuir isotherm adsorption model. This study provides a route for the synthesis of oxides with large specific surface areas and obtained an adsorbent with superior adsorption capacity.

Received 7th November 2018
Accepted 22nd December 2018

DOI: 10.1039/c8ra09199d

rsc.li/rsc-advances

Introduction

Most organic dyes are difficult to handle as contaminants in wastewater.[1–8] For water reuse, the effective removal of dyes from wastewater is of great significance.[9–12] Owing to high efficiency, speed, and low energy requirements, adsorption is a universal and advantageous approach to removing dyes from aqueous systems among various other methods.[13–15] However, ordinary adsorbents have a limited adsorption capacity and low adsorption rate.[16] As a traditional material used in wastewater treatment, MgO is an indispensable substance that is low-cost, eco-friendly, nontoxic, and economical.[17–21] In the past few decades, many studies have reported the excellent properties of nanomaterials resulting from their nanoscale size, with many showing extremely superior performance in various fields.[22–24] Accordingly, efforts have been made to prepare nanoscale MgO using effective routes such as hydrothermal strategies and the sol–gel method.[1,25–27] Studies over many years have found that the particle size and specific surface area are both significant factors affecting the adsorption performance.[1,25,26,28] To improve the adsorption properties, decreasing the size and increasing the specific surface area using template agents or surfactants has become the general strategy. Furthermore, the surface basicity has also been found to have a crucial effect on the adsorption capacity.[29] Lamellar MgO nanostructures with alkaline surfaces have been successfully synthesized *via* hydrothermal synthesis, and demonstrated a superior adsorption performance towards Congo red solutions with an adsorption capacity of 2650 mg g^{-1}.[30] Other MgO nanomaterials with different morphologies have also been synthesized in solution.[25–29] However, their synthesis usually requires complex preparation processes owing to multistep synthetic operations under solution conditions, resulting in unnecessary environmental pollution from the organic agents. Therefore, a simple and low-pollution method for synthesizing nanoscale MgO materials is needed for the study of adsorptive materials with excellent properties.

Herein, we designed a convenient and efficient strategy for synthesizing MgO nanoparticles with a small size, large specific surface area, and suitable surface basicity using a solvent-free strategy under ambient conditions. This preparation method is green, non-polluting, and simple.[31–33] Notably, without using any organic solvents, template agents, or surfactants, the obtained MgO nanoparticles with sizes of 10–20 nm and a specific surface area of 213 $m^2\ g^{-1}$ exhibited a high adsorption capacity of 2375 mg g^{-1} for Congo red from the dye solution. Therefore, this material was a superior adsorbent for removing Congo red from wastewater. Furthermore, the MgO nanoparticles also adsorbed toxic metal ions from dilute solution. MgO nanoparticles prepared using this facile solid-state chemical route are expected to be promising adsorbents for wastewater treatment.

Key Laboratory of Energy Materials Chemistry, Ministry of Education, Key Laboratory of Advanced Functional Materials, Autonomous Region, Institute of Applied Chemistry, Xinjiang University, Urumqi, 830046 Xinjiang, P. R. China. E-mail: caoyali523@163.com; Fax: +86-991-8588883; Tel: +86-991-8583083

† Electronic supplementary information (ESI) available. See DOI: 10.1039/c8ra09199d

Experimental

Synthesis of MgO nanoparticles

All products were prepared using a solid-state chemical reaction. All reagents were of analytical grade from commercial sources and used as received without further purification. Detailed experimental procedures are provided below.

In a typical synthesis of MgO nanoparticles, magnesium acetate tetrahydrate ($Mg(OAc)_2 \cdot 4H_2O$, 10 mmol) was ground to a fine powder in an agate mortar and mixed with oxalic acid dihydrate powder ($H_2C_2O_4 \cdot 2H_2O$, 15 mmol) prepared by grinding in another mortar. The obtained blended powder was ground to ensure adequate contact of the reactants for the solid-state chemical reaction under ambient conditions through a wetting process until a dry white powder was obtained. Some of the as-obtained dry white powder was sealed in a 50 mL conical flask, heated in a water bath at 60 °C for 24 h, and then rinsed with distilled water several times and dried at ambient temperature for 12 h. Another portion of the as-obtained dry white powder was directly calcined at 450, 550, 650, and 750 °C for 2 h under an air atmosphere to produce MgO nanoparticles with heating rates of 2, 5, and 10 °C min^{-1}, respectively.

Oxalic acid dihydrate ($H_2C_2O_4 \cdot 2H_2O$, 15 mmol) was replaced with NaOH (30 mmol). After rinsing and drying as above, the as-obtained mixture was calcined at 450 °C for 2 h under an air atmosphere with a heating rate of 2 °C min^{-1} to produce MgO nanoparticles. Other experimental steps were the same as detailed above.

The as-prepared MgO nanoparticles were studied as Congo red adsorbents. After adsorption, the MgO nanoparticles were regenerated by evaporating Congo red at 450 °C for 2 h under an air atmosphere using a heating rate of 5 °C min^{-1}.

Characterization

X-ray diffraction (XRD, Bruker D8 Advance) of the as-obtained target product was conducted using Cu-Kα radiation (λ = 1.54056 Å) with an operating voltage of 40 kV and a working current of 40 mA in the θ range of 10–80° at a scanning rate of 2° min^{-1}. The morphology was observed by field emission scanning electron microscopy (FESEM, Hitachi S-4800H) using an accelerating voltage of 5 kV, by transmission electron microscopy (TEM, Hitachi H-600) using an accelerating voltage of 120 kV, and by high-resolution transmission electron microscopy (HR-TEM, JEOL JEM-2010F) using an accelerating voltage of 200 kV. UV-vis absorption spectra of the as-generated adsorbents were obtained using a Hitachi U-3010 spectrophotometer at 200–800 nm. Temperature-programmed desorption of CO_2 (CO_2-TPD) was measured to characterize the basicity of the target MgO products placed in a Chembet Pulsar TPR/TPD reactor. First, samples (600 mg) were heated to 750 °C at a rate of 15 °C min^{-1} under Ar flow (50 mL min^{-1}) and held at that temperature for 1 h to purify the surface. After cooling to 50 °C under Ar flow (50 mL min^{-1}), the target samples were exposed to CO_2 gas (50 mL min^{-1}) for 0.5 h. The target samples were then purged under an Ar atmosphere (50 mL min^{-1}) for 1 h and heated to 800 °C at a rate of 15 °C min^{-1}. N_2 absorption–desorption tests were conducted to determine the specific surface area, pore size, and pore volume of the products using the Brunauer–Emmett–Teller (BET) and Barrett–Joyner–Halenda (BJH) methods on a quantachrome (Autosorb-iQ2) automated sorption system. Fourier transform infrared (FTIR) spectra of the generated samples were recorded with a Bruker VERTEX 70 spectrometer in the range 4000 to 400 cm^{-1} using the KBr method. Thermogravimetric analysis (TGA) and differential scanning calorimetry (DSC) curves of the precursors were acquired on a NETZSCH STA 449F3 simultaneous thermal analyzer at a heating rate of 10 °C min^{-1} from 50 to 700 °C under an air atmosphere. Inductively coupled plasma optical emission spectroscopy (ICP-OES) was conducted using a full-spectrum direct-reading dry-coupled plasma emission spectrometer (Optima 8000, PerkinElmer, USA).

Adsorption experiments

All adsorption experiments were performed by dispersing the as-synthesized MgO particles (10 mg) in Congo red (CR) aqueous solution (20 mL) in a 50 mL vessel, which was covered to avoid water loss through evaporation, with regular shaking on a Wrist Action shaker (Burrel, Model 75-BB) at natural pH and room temperature for 60 min. The Congo red solutions with initial concentrations ranging from 400 to 1400 mg L^{-1} were obtained by completely dissolving Congo red in aqueous solution. At several time intervals, a 2 mL aliquot of the mixture was collected and separated to remove the MgO adsorbent. To monitor the adsorption process, the supernatant was then subjected to UV-vis spectrometry (Thermo Fisher Scientific Inc., Canada) at 499 nm to measure the characteristic adsorption of CR.

The adsorption properties of products prepared at different calcination temperatures were examined in CR solution with a concentration of 400 mg L^{-1}. MgO synthesized from different starting materials was investigated in CR solution with a concentration of 600 mg L^{-1}. Other operating specifications were as detailed above.

The adsorption capacity of as-prepared MgO, Q_t (adsorbed amount of nanoparticles in the CR solution), was calculated using eqn (1):

$$Q_t = (C_0 - C_t)V/m \quad (1)$$

where Q_t is the adsorption capacity of the used MgO (mg g^{-1}), C_0 and C_t are the concentrations of Congo red before and after adsorption, respectively (mg L^{-1}), V is the solution volume (L), and m is the mass of used MgO sample (g).

Pseudo-first-order (eqn (2)) and pseudo-second-order (eqn (3)) kinetic models were examined in the adsorption of Congo red by as-prepared MgO, with the kinetic data interpreted as follows:

$$\log(q_e - q_t) = \log q_e - k_1 t/2.303 \quad (2)$$

$$t/q_t = 1/(k_2 q_e^2) + t/q_e \quad (3)$$

where q_e is the adsorption capacity of MgO particles at equilibrium (mg g^{-1}), q_t is the adsorption capacity (mg g^{-1}) of MgO

particles at any time t (min), and k_1 (min^{-1}) and k_2 (g mg^{-1} min^{-1}) are the pseudo-first-order and pseudo-second-order rate constants, respectively.

The Langmuir and Freundlich adsorption isotherms (eqn (4) and (5), respectively) were used to describe the Congo red adsorption process on as-obtained MgO particles, as follows:

$$q_e = q_m b C_e/(1 + bC_e) \quad (4)$$

$$\ln q_e = 1/n(\ln C_e) + \ln k_f \quad (5)$$

where q_m is the Langmuir adsorption capacity corresponding to complete full monolayer coverage of the adsorbent surface (mg g^{-1}), C_e is the equilibrium concentration of Congo red in solution after adsorption (mg L^{-1}), b is the Langmuir equilibrium constant related to affinity (L mg^{-1}), k_f is an indicator of the adsorption capacity, and n is the Freundlich adsorption intensity.

We also measured the adsorption behavior of toxic ions, such as Co^{2+}, Cu^{2+}, and Ni^{2+}. The experimental parameters used were the same as above. Acetate solutions with initial concentrations of 1000 mg L^{-1} were obtained by dissolving acetate into aqueous solution, ensuring complete dissolution. At several time intervals, a 2 mL aliquot of the mixture was collected, centrifuged, and passed through a filter membrane to remove MgO adsorbents. The concentration of metal ions remaining in the resulting supernatant was then measured by ICP-OES to monitor the adsorption process.

Results and discussion

Characterization of MgO nanoparticles

The overall synthetic procedure is depicted in Fig. 1a. The synthesis of MgO nanoparticles was achieved through the simple solid-state chemical reaction between magnesium acetate and oxalic acid. The typical SEM image in Fig. 1b shows the resulting MgO, in which the uniform particles were directly observed. Fig. 1c shows TEM and HRTEM images of the MgO nanoparticles with average particle diameters of approximately 10 nm, indicating a distinct lattice space of 0.21 nm, which corresponded well with the normal (200) plane, and was consistent with reported data.[30] MgO nanoparticles with an average diameter of about 10 nm had been successfully prepared by a facile solvent-free strategy using the reaction between $Mg(OAc)_2$ and $H_2C_2O_4$. Compared with the particles size of MgO prepared using other synthetic methods in previous reports, the obtained MgO nanoparticles were much smaller, probably owing to the different microenvironment of the direct-contact solid-state chemical reaction relative to solution synthesis.[11,31–34]

The crystal phase of the as-obtained product was analyzed by XRD, as shown in Fig. 1d. All XRD diffraction peaks of the as-prepared samples were in good agreement with the diffraction peaks of the main characteristic planes, (200), (220), and (222), of MgO (JCPDS card no. 74-1225). Furthermore, no other impurities were detected in the XRD pattern, which showed that pure MgO could be successfully obtained using this solvent-free

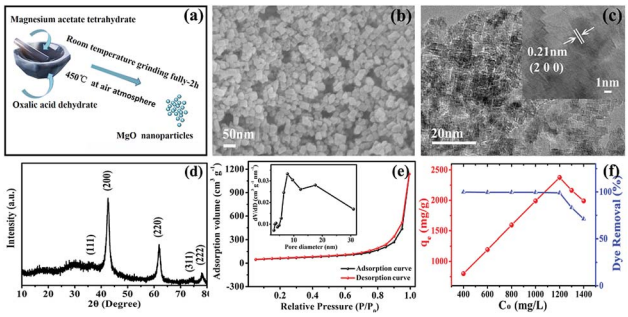

Fig. 1 (a) Fabrication scheme, (b) SEM image, (c) TEM and HR-TEM (inset) images, (d) XRD pattern, (e) N_2 adsorption–desorption isotherms and pore size distribution curves (inset) and (f) adsorption isotherm of Congo red on the MgO nanoparticles.

approach. Simultaneously, the MgO diffraction peaks were broad, indicating that the MgO samples had small crystallite sizes,[35] calculated as 10.5 nm using the Scherrer equation. This was consistent with the TEM results.

As shown in Fig. 1e, the N_2 adsorption–desorption isotherm and corresponding pore size distribution curve (inset) of the as-synthesized MgO products exhibited a typical type-IV isotherm with a significant H3 hysteresis loop, which are typical characteristics of a porous structure.[36] A clear H3 hysteresis loop was observed at medium relative pressure (P/P_0) range, which confirmed the presence of considerable mesopores in the MgO nanoparticles. Analysis results for the N_2 adsorption–desorption isotherm were in good agreement with the fact that abundant mesopores existed, as expressed on the pore size distribution curve (inset). Furthermore, an uncommon phenomenon appeared to cause the isotherm destination to turn upward at the high relative pressure stage, which was probably due to pores created by particles stacking. The test results showed that the BET specific surface area as-synthesized MgO was 213.4 m^2 g^{-1}, which was slightly higher than the specific surface area values of other MgO products reported in the literature, as shown in Table S1 (ESI†).

The adsorption properties of the as-generated MgO nanoparticles were evaluated in the removal of CR (Congo red) from solution, which is a typical representative of most experimental wastewater treatments, simulating practical applications at natural pH and room temperature. Fig. 1f shows the adsorption isotherm of CR on MgO nanoparticles, suggesting that the as-prepared products had excellent adsorption properties. Clearly, continuously increasing the initial concentration of the Congo red solution below 1200 mg L^{-1} resulted in a concentration-dependent adsorption capacity on the as-obtained MgO nanoparticles. This trend showed a linear increase up to a maximum value at 2375 mg g^{-1} within an adsorption time of 1 h and then slightly decreased at the initial concentration above 1200 mg L^{-1}. The superior maximum adsorption value of 2375 mg g^{-1} towards CR adsorption in solution at various initial concentrations in the range of 400–1400 mg L^{-1} for 1 h at natural pH and room temperature on the as-obtained MgO adsorbent was nearly equal to the reported superhigh adsorption capacity,[1,30] which was superior to that in most

reports.[16,25,28,37] This showed that MgO nanoparticles prepared *via* the facile solvent-free chemical reaction manifested outstanding adsorption properties.

Factors influencing adsorption performance on MgO nanoparticles

To investigate the effect of experimental parameters on the adsorption performance of target sample MgO nanoparticles, more than one experimental parameter is discussed. The experimental results showed that changing the experimental parameters had a great influence on the Congo red removal capacity. In our work, magnesium acetate tetrahydrate ($Mg(OAc)_2 \cdot 4H_2O$) and oxalate ($H_2C_2O_4 \cdot 2H_2O$) or NaOH was used to prepare the precursor (Fig. S1 in ESI†) and then obtain MgO target products (Fig. S2†) after calcination. The precursor showed uniform nanoparticles (Fig. S3†). The grain size of about 10.5 nm, calculated using the Debye–Scherrer formula, for the sample prepared from oxalate ($H_2C_2O_4 \cdot 2H_2O$) was smaller than that prepared from NaOH as the raw material, which might result from the slower reaction rate between $Mg(OAc)_2 \cdot 4H_2O$ and $H_2C_2O_4 \cdot 2H_2O$, in good accordance with the TEM images in Fig. S4.† The N_2 adsorption–desorption isotherm are shown in Fig. 2a. The specific surface area of MgO nanoparticles fabricated with oxalate was larger than that fabricated with NaOH as the raw material (Table S2†). Generally, the adsorption performance was well correlated with the surface area, with a larger specific surface area resulting better adsorption properties. Fig. 2b shows the influence of different raw materials on the Congo red (CR) adsorption properties of the MgO sample. The intensity of the characteristic adsorption peak occurred at approx. 498 nm in the UV-vis spectrum of MgO prepared with NaOH for Congo red removal was stronger than for that prepared with oxalate as the raw material. The inset in Fig. 2b shows a picture of CR dye after the adsorption process with MgO synthesized using different materials. The color changed from transparent to red when the materials were changed from oxalate to NaOH. Clearly, the MgO products prepared from $H_2C_2O_4 \cdot 2H_2O$ exhibited much better adsorption properties towards Congo red in solution, which might be due to another impact factor, namely, the surface basicity of MgO. Generally, the pH value of Congo red is 4.1, which is weakly acidic, while MgO, with an isoelectric point of approx. 12, is alkaline. In solution, CR would be adsorbed to the surface of MgO through a neutralization reaction.[28] To determine the surface basicity of the prepared MgO samples, temperature-programmed desorption (TPD) of CO_2 curves were obtained, as shown in Fig. 2c. Two CO_2 desorption peaks were observed, which showed that the basic active sites existed on sample surface. According to other reports, the basic sites were divided into three types in increasing order of base strength, namely, hydroxyl groups on MgO surfaces, oxygen in Mg^{2+} and O^{2-} pairs, and low coordination oxygen anions. The CO_2 desorption peaks were mainly below 600 °C.[37–40] Clearly, the MgO particles prepared with different raw materials exhibited weak and medium basicity. Both the peak strength (Fig. 2b) and peak area can describe the quantitative change in CO_2 desorption for samples generated with oxalate, which were both stronger than those of NaOH as the raw material. The adsorption properties were related to the grain size, specific surface area, and surface basic active sites. The smaller particle size resulted in a larger surface area and more exposed basic active sites on the surface, which exhibited better adsorption performance. The adsorption capacity (Fig. S5†) of MgO prepared using NaOH was only 725 mg g^{-1}, which was much lower than that prepared from $H_2C_2O_4 \cdot 2H_2O$ as the raw material.

Another important experimental parameter is calcination temperature, which can affect the grain size, specific surface area, and surface basicity of the as-synthesized MgO nanoparticles. MgO was obtained by calcination of the precursors at selected temperatures ranging from 450 to 750 °C (Fig. S6 and S7†). Fig. 3a shows the influence of calcination temperature on the adsorption efficiency of MgO nanoparticles. Obviously, as the temperature increased from 450 to 750 °C, the adsorption performance towards CR showed a continuous decrease in adsorption capacity. Fig. 3b showed that as the temperature increased, the final color after the adsorption process became lighter. The CO_2-TPD curves are described in Fig. 3c. The peak strength gradually decreased with increasing calcination temperature from 450 to 750 °C, which reflected that MgO had medium basicity within the range of 270–440 °C. Fig. 3c and

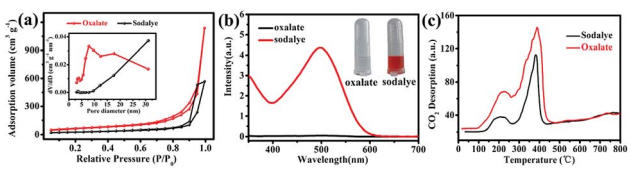

Fig. 2 (a) N_2 adsorption–desorption isotherms and pore size distribution curves (inset), (b) UV-vis spectra of initial CR solutions (600 mg L^{-1}) treated with MgO (10 mg) and (c) CO_2-TPD profiles of MgO nanoparticles prepared from different materials.

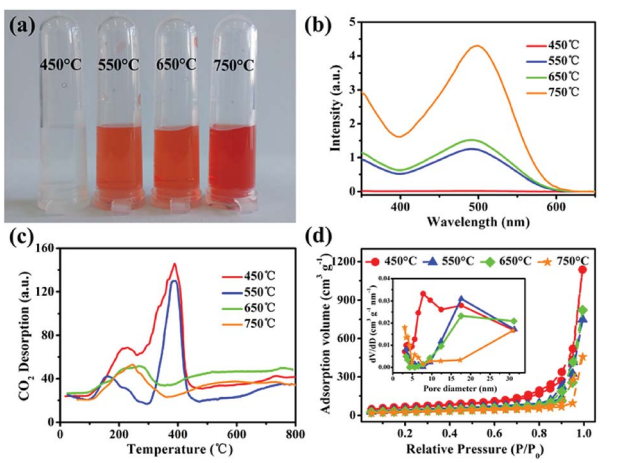

Fig. 3 (a) Photograph and (b) UV-vis spectra of initial CR solutions (400 mg L^{-1}), (c) CO_2-TPD profiles, and (d) N_2 adsorption–desorption isotherms and pore size distribution curves (inset) of MgO nanoparticles acquired from the calcination of precursors at various temperatures in the range 450–750 °C.

d show that both the specific surface area and surface alkalinity of the samples decreased with increasing calcination temperature. Therefore, a higher calcination temperature resulted in a larger particle size (Fig. S8 and S9†) and smaller specific surface area (Table S3†). Accordingly, the surface basic active sites were less exposed and the adsorption performance was worse. Owing to these factors, the MgO nanoparticles obtained at a calcination temperature of 450 °C showed the most efficient adsorption in CR solutions. In this work, we also explored the experimental parameters of the water bath and the heating rate to fabricate MgO nanoparticles. The adsorption results indicated that, as shown in Fig. S10 and S11,† the MgO nanoparticles prepared by increasing the temperature at a rate of 5 °C min^{-1} without the water bath process exhibited optimal adsorption properties.

Adsorption performance of MgO nanoparticles

In this work, the solvent-free chemical synthesis resulted in a small particle size and high specific surface area. To further examine the performance of as-obtained MgO towards CR removal, we investigated the adsorption process for adsorbing CR on MgO nanoparticles at various initial concentrations, ranging from 600 to 1200 mg L^{-1}, with an adsorbent dosage of only 10 mg in 20 mL of CR solution at room temperature and natural pH. As shown in Fig. 4, the adsorption rates were markedly fast in the first 5 min at all CR concentrations, with adsorption processes almost complete within 30 min. This demonstrated the ultra-rapid adsorption rate of these MgO nanoparticles in CR solution. With increasing initial CR concentration, the adsorption rate gradually decreased. MgO generated a remarkable adsorption capacity of 2375 mg g^{-1} for CR removal within an adsorption time of 60 min at an initial concentration of 1200 mg L^{-1} in CR solution.

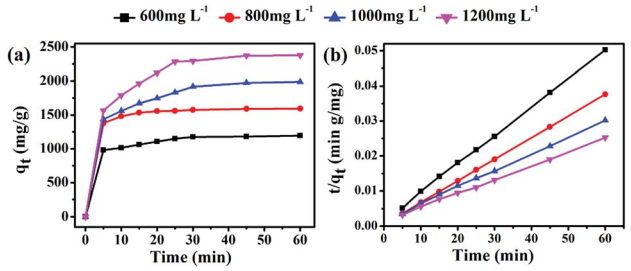

Fig. 4 (a) Time profiles of CR adsorption on as-obtained MgO (10 mg) at different initial concentrations (600–1200 mg L^{-1}) and (b) the derived pseudo-second-order kinetics plots of CR adsorption.

To gain insight into the transient kinetic adsorption behavior of CR removal on MgO, the pseudo-first-order and pseudo-second-order kinetic models were employed, with detailed adsorption kinetic parameters shown in Table 1. When the adsorption process fitted the pseudo-first-order kinetic model, the calculated values (q_e) were lower than the experimental values. When the pseudo-second-order kinetic model was used, the calculated values (q_e) were quite close to the experimental values, or even slightly higher, probably owing to the transient kinetic adsorption behavior. The correlation coefficients (R^2 > 0.998) of the pseudo-second-order kinetic model, according to comparisons of the correlation coefficients, were all somewhat higher than those of the pseudo-first-order kinetic model, suggesting that the adsorption process of CR (Congo red) on as-synthesized MgO better obeyed the pseudo-second-order kinetic model than the pseudo-first-order kinetic model. This indicated that a chemical adsorption process was dominant in the adsorption process.

To further understand the adsorption process in CR removal by as-prepared MgO, the relationship between the adsorption capacity and equilibrium concentration of the CR solution was measured using Langmuir and Freundlich isotherms experiments, respectively, as shown in Fig. S12.† The corresponding parameters and correlation coefficients (R^2) are listed in Table S4.† The adsorption process clearly followed the Langmuir isotherm, with correlation coefficients (R^2) of 0.9916, rather than the Freundlich isotherm, with correlation coefficients (R^2) of 0.9891, indicating a monolayer adsorption process.

To date, the adsorption capacities of many adsorbents for CR removal were usually below 2000 mg g^{-1}. Clearly, the adsorption capacity of MgO in this study is notable among most data reported in previous articles, as shown in Table S5.† This reflected that MgO prepared using the solvent-free route exhibited an unexceptionable adsorption capacity, and is expected to be a prospective adsorbent for Congo red in wastewater treatment.

Analysis of adsorption process

To clarify the adsorption process of Congo red on MgO nanoparticles, FT-IR characterization was performed. The excellent adsorption performance of MgO was highly correlated with oxygen-containing functional groups on the MgO surface, which act as anchoring sites for Congo red molecules. It has been well documented that the oxygen atom of the S=O group

Table 1 Adsorption parameters for the adsorption of CR on MgO nanoparticles

	Pseudo-first order model				Pseudo-second order model			
Initial concentration (mg L^{-1})	Experimental q_e (mg g^{-1})	Calculated q_e (mg g^{-1})	K_1 (g mg^{-1} min^{-1})	R^2	Experimental q_e (mg g^{-1})	Calculated q_e (mg g^{-1})	K_2 (g mg^{-1} min^{-1})	R^2
600	1194.15	1135.97	0.354	0.9779	1194.15	1231.42	4.3×10^{-4}	0.9995
800	1593.46	1561.82	0.412	0.9968	1593.46	1617.86	7.2×10^{-4}	0.9999
1000	1987.85	1861.26	0.241	0.9632	1987.85	2100.21	1.4×10^{-4}	0.9988
1200	2376.67	2279.87	0.182	0.9712	2376.67	2541.04	1.1×10^{-4}	0.9987

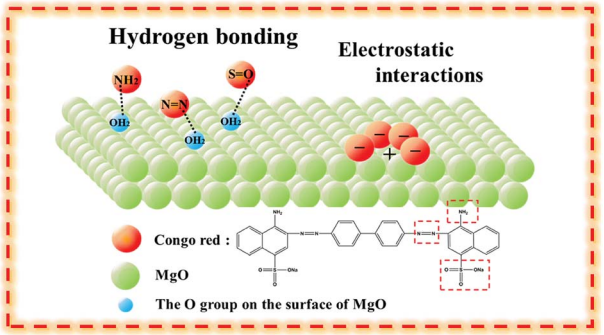

Fig. 5 Schematic diagram of CR on MgO nanoparticles through hydrogen bonding and electrostatic interactions.

can be used as a hydrogen bond acceptor to form intermolecular hydrogen bonds with H atoms of hydroxyl groups on the surface of MgO.[41] In this study, the FT-IR spectrum in Fig. S13† shows a peak at ~1041 cm^{-1} that could be assigned to the stretching vibration of S=O in Congo red. After adsorbing CR, the peak clearly sharpened and significantly increased in intensity, which was attributed to the hydrogen bond formation, confirming that Congo red could become attached to the MgO surface. FT-IR spectra after the adsorption process showed a slight increase in the peak intensity at 3475 cm^{-1}, corresponding to $-NH_2$ group of CR, which might be attributed to hydrogen bond interactions between the nitrogen atom of $-NH_2$ group and the hydrogen atom of –OH group on the MgO surface.[42] Meanwhile, the position of the –N=N– stretching vibration peak increased to 2000 cm^{-1} owing to conjugation of the double bond and aromatic ring. The peak narrowed and sharpened after adsorption owing to hydrogen bonding between the nitrogen atom of –N=N– group and the hydrogen atom of the –OH group on the MgO surface, which demonstrated that the –N=N– group was attached to the MgO surface.

The above analysis confirmed that the excellent adsorption properties of MgO nanoparticles resulted from hydrogen bonding (Fig. 5). Furthermore, the isoelectric point of the adsorbent was higher than the pH value of the dye solution, meaning that the adsorbent will be positively charged and can absorb the anionic dye molecules *via* electrostatic interactions.[1] The isoelectric point of MgO at natural pH is 12.1–12.7. In solution, the natural pH of Congo red as an anionic dye is approx. 7. As the isoelectric point of MgO is higher than the natural pH of CR solution, MgO with a positive surface charge could readily adsorb the anionic dye Congo red. Therefore, we concluded that the superior adsorption performance of MgO nanoparticles was associated with both hydrogen bonding and electrostatic interactions with the surface.

Regeneration and toxic metal ion adsorption applications

The reusability of adsorbents is also significant for applications. The adsorption behavior after recycling and regenerating MgO nanoparticles was investigated. As shown in Fig. 6a, after the third cycling experiment, the removal rate of Congo red by MgO nanoparticles was approximately 75%, probably owing to MgO

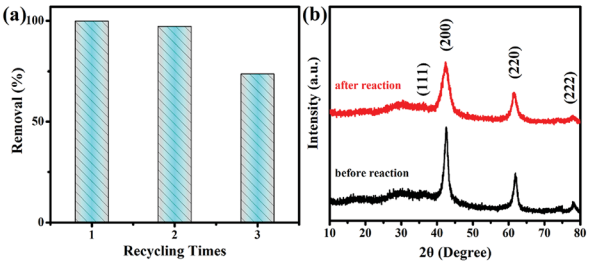

Fig. 6 (a) Recycle adsorption experiments and (b) XRD patterns of MgO nanoparticles before and after adsorption.

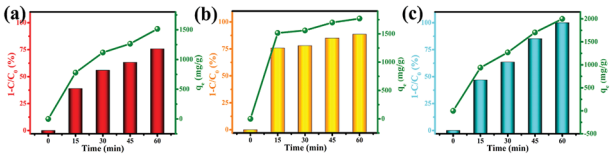

Fig. 7 Toxic ion adsorption experiments for (a) Co^{2+}, (b) Cu^{2+}, and (c) Ni^{2+} on MgO nanoparticles.

nanoparticle agglomeration. SEM images (Fig. S14†) clearly showed the change from uniform particles to agglomeration, which were the real situations before and after adsorption. A reusability experiment was also conducted, as shown in Fig. S15,† by heating the static adsorbent after adsorption at 450 °C for 2 h in air, which favored thermal decomposition of the adsorbate as gases. The XRD pattern in Fig. 6b shows the adsorbent after heat treatment, which retained the same diffraction peaks as the initial adsorbent. Toxic ions are also difficult to treat as environmental pollutants.[43,44] The MgO nanoparticles also possessed adsorption properties for toxic ions, including cobalt, copper, and nickel, as shown in Fig. 7. Therefore, these MgO nanoparticles showed superior adsorption performance as a promising material for practical applications.

Conclusions

Herein, we prepared MgO nanoparticles with a large specific surface area of 213 $m^2\ g^{-1}$ using a simple solid-state method without using any liquid solvent, template agent, or surfactant. The MgO nanoparticles showed a robust adsorption capacity of 2375 mg g^{-1} towards Congo red. The raw materials and calcination temperature affected the particle size, specific surface area, and surface basicity, which further influenced the adsorption properties. The remarkable adsorption capacity was attributed to hydrogen bonding between the hydrogen atoms of –OH groups on the MgO surface and nitrogen or oxygen atoms of characteristic functional groups in Congo red, and electrostatic interactions between the positively charged MgO surface and anionic Congo red dye. The adsorption behavior followed pseudo-second-order kinetic and Langmuir isotherm adsorption models. The superior adsorption properties of the MgO nanoparticles make them a promising adsorbent for purifying wastewater containing dyes.

Conflicts of interest

There are no conflicts to declare.

Acknowledgements

This research was financially supported by the National Natural Science Foundation of China (U1503392, 21771157, and 21766036), the Scientific Research Program of the Higher Education Institution of Xinjiang (XJEDU2016S040), the Natural Science Foundation of Xinjiang Uygur Autonomous Region (2017XS01 and 2017D01C033), and the Doctoral Fund of Xinjiang University (BS160255).

Notes and references

1 P. Tian, X. Y. Han, G. L. Ning, H. X. Fang, J. W. Ye, W. T. Gong and Y. Lin, *ACS Appl. Mater. Interfaces*, 2013, **5**, 12411–12418.
2 G. Crini, *Bioresour. Technol.*, 2006, **97**, 1061–1085.
3 M. Alkan, S. Çelikçapa, Ö. Demirbaş and M. Doğan, *Dyes Pigm.*, 2005, **65**, 251–259.
4 Y. D. Han, W. W. Li, J. Zhang, H. Meng, Y. Xu and X. Zhang, *RSC Adv.*, 2015, **5**, 104915–104922.
5 T. T. Li, Y. M. Liu, T. Wang, Y. L. Wu, Y. L. He, R. Yang and S. R. Zheng, *Microporous Mesoporous Mater.*, 2018, **272**, 101–108.
6 M. P. Wei, H. Chai, Y. L. Cao and D. Z. Jia, *J. Colloid Interface Sci.*, 2018, **524**, 297–305.
7 J. Y. Luo, Y. R. Lin, B. W. Liang, Y. D. Li, X. W. Mo and Q. G. Zeng, *RSC Adv.*, 2015, **5**, 100898–100904.
8 F. Ren, Z. Li, W. Z. Tan, X. H. Liu, Z. F. Sun, P. G. Ren and D. X. Yan, *J. Colloid Interface Sci.*, 2018, **532**, 58–67.
9 Y. Z. Li, Y. L. Cao and D. Z. Jia, *CrystEngComm*, 2016, **18**, 8465–8471.
10 J. Xie, Y. L. Cao, D. Z. Jia, Y. Z. Li, K. Wang and H. Xu, *Sci. Rep.*, 2017, **7**, 12365.
11 Z. L. Liang, Y. L. Cao, Y. Z. Li, J. Xie, N. N. Guo and D. Z. Jia, *Appl. Surf. Sci.*, 2016, **390**, 78–85.
12 J. Xie, Y. L. Cao, D. Z. Jia, H. Y. Qin and Z. T. Liang, *Catal. Commun.*, 2015, **69**, 34–38.
13 X. M. Liu, C. Niu, X. P. Zhen, J. D. Wang and X. T. Su, *J. Colloid Interface Sci.*, 2015, **452**, 116–125.
14 K. Peng and H. M. Yang, *Chem. Commun.*, 2017, **53**, 6085–6088.
15 A. R. Auxilio, P. C. Andrews, P. C. Junk and L. Spiccia, *Dyes Pigm.*, 2009, **81**, 103–112.
16 L. H. Ai, H. T. Yue and J. Jiang, *Nanoscale*, 2012, **4**, 5401–5408.
17 S. Purwajanti, H. W. Zhang, X. D. Huang, H. Song, Y. N. Yang, J. Zhang, Y. T. Niu, A. K. Meka, O. Noonan and C. Z. Yu, *ACS Appl. Mater. Interfaces*, 2016, **8**, 25306–25312.
18 J. Schneider, F. Kollhoff, J. Bernardi, A. Kaftan, J. Libuda, T. Berger, M. Laurin and O. Diwald, *ACS Appl. Mater. Interfaces*, 2015, **7**, 22962–22969.
19 L. Sharma and R. Kakkar, *ACS Appl. Mater. Interfaces*, 2017, **9**, 38629–38642.
20 S. L. Yang, P. P. Huang, L. Peng, C. Y. Cao, Y. N. Zhu, F. Wei, Y. B. Sun and W. G. Song, *J. Mater. Chem. A*, 2016, **4**, 400–406.
21 H. R. Mahmoud, S. M. Ibrahim and S. A. El-Molla, *Adv. Powder Technol.*, 2016, **27**, 223–231.
22 B. Eckhardt, E. Ortel, J. Polte, D. Bernsmeier, O. Gorke, P. Strasser and R. Kraehnert, *Adv. Mater.*, 2012, **24**, 3115–3119.
23 F. Gherardi, S. Goidanich, V. Dal Santo and L. Toniolo, *Angew. Chem., Int. Ed.*, 2018, **57**, 7360–7363.
24 C. Y. Hui, M. Liu, Y. F. Li and J. D. Brennan, *Angew. Chem., Int. Ed.*, 2018, **57**, 4639–4643.
25 J. Xu, D. F. Xu, B. C. Zhu, B. Cheng and C. J. Jiang, *Appl. Surf. Sci.*, 2018, **435**, 1136–1142.
26 M. Q. Hu, X. L. Yan, X. Y. Hu, J. J. Zhang, R. Feng and M. Zhou, *J. Colloid Interface Sci.*, 2018, **510**, 111–117.
27 S. Nayak, A. C. Pradhan and K. M. Parida, *Inorg. Chem.*, 2018, **57**, 8646–8661.
28 X. H. Shi, J. J. Ban, L. Zhang, Z. P. Sun, D. Z. Jia and G. C. Xu, *RSC Adv.*, 2017, **7**, 16189–16195.
29 Z. Q. Bai, Y. J. Zheng and Z. P. Zhang, *J. Mater. Chem. A*, 2017, **5**, 6630–6637.
30 X. M. Liu, C. Niu, X. P. Zhen, J. D. Wang and X. T. Su, *J. Mater. Res.*, 2015, **30**, 1639–1647.
31 Y. Z. Li, Y. L. Cao and D. Z. Jia, *J. Mater. Chem. A*, 2014, **2**, 3761–3765.
32 K. Wang, Y. L. Cao, J. D. Hu, Y. Z. Li, J. Xie and D. Z. Jia, *ACS Appl. Mater. Interfaces*, 2017, **9**, 16128–16137.
33 H. Y. Qin, Y. L. Cao, J. Xie, H. Xu and D. Z. Jia, *Sens. Actuators, B*, 2017, **242**, 769–776.
34 H. Xu, J. Xie, W. Jia, G. M. Wu and Y. L. Cao, *J. Colloid Interface Sci.*, 2018, **516**, 511–521.
35 B. F. Machado, M. Oubenali, M. Rosa Axet, T. Trang Nguyen, M. Tunckol, M. Girleanu, O. Ersen, I. C. Gerber and P. Serp, *J. Catal.*, 2014, **309**, 185–198.
36 Z. W. Li, N. N. Chen, H. Y. Mi, J. H. Ma, Y. H. Xie and J. S. Qiu, *Chem.–Eur. J.*, 2017, **23**, 13474–13481.
37 J. P. Dhal, M. Sethi, B. G. Mishra and G. Hota, *Mater. Lett.*, 2015, **141**, 267–271.
38 A. El-Qanni, N. N. Nassar and G. Vitale, *RSC Adv.*, 2017, **7**, 14021–14038.
39 F. J. Li, H. Q. Li, L. G. Wang, P. He and Y. Cao, *Catal. Sci. Technol.*, 2015, **5**, 1021–1034.
40 T. Selvamani, T. Yagyu, S. Kawasaki and I. Mukhopadhyay, *Catal. Commun.*, 2010, **11**, 537–541.
41 J. Ma, F. Yu, L. Zhou, L. Jin, M. X. Yang, J. S. Luan, Y. H. Tang, H. B. Fan, Z. W. Yuan and J. H. Chen, *ACS Appl. Mater. Interfaces*, 2012, **4**, 5749–5760.
42 R. M. Mohamed, A. Shawky and I. A. Mkhalid, *J. Phys. Chem. Solids*, 2017, **101**, 50–57.
43 L. Aboutorabi, A. Morsali, E. Tahmasebi and O. Büyükgüngor, *Inorg. Chem.*, 2016, **55**, 5507–5513.
44 J. Ai, F. Y. Chen, C. Y. Gao, H. R. Tian, Q. J. Pan and Z. M. Sun, *Inorg. Chem.*, 2018, **57**, 4419–4426.